Engineering Analysis with Boundary Elements 169 (2024) 105976

Contents lists available at ScienceDirect

Engineering Analysis with Boundary Elements

journal homepage: www.elsevier.com/locate/enganabound

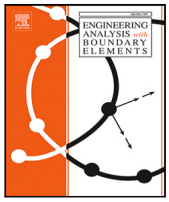

Optimisation of open pit slope design considering groundwater effects using particle swarm optimisation and scaled boundary finite element method

Dakshith Ruvin Wijesinghe [a], Ethmadalage Perera [b], Ean Hin Ooi [c], Sundararajan Natarajan [d], Taghi Sherizadeh [a], Ean Tat Ooi [b,*]

[a] Department of Mining and Explosive Engineering, Missouri University of Science and Technology, Rolla, MO 65409, USA
[b] Institute of Innovation Science and Sustainability, Federation University Australia, Ballarat 3350, Australia
[c] School of Engineering, Monash University-Malaysia, Bandar Sunway, 47500 Selangor, Malaysia
[d] Integrated Modelling and Simulation Lab, Department of Mechanical Engineering, Indian Institute of Technology, Madras, Chennai, 600036, India

ARTICLE INFO

Keywords:
Particle swarm optimisation
Slope optimisation
Slope stability
Scaled boundary finite element method
Groundwater

ABSTRACT

Slopes are a crucial structures in open pit mines. Their design has implications on the economic, safety and environmental operation of the mining industry. Designing stable slopes can be challenging due to the complexities introduced by the stratigraphy and hydrology of the strata. With rising commodity costs and inflation rates, mining operating costs are increasing. Reducing operational costs is necessary for mining industries to remain competitive. While steepening the pit slope can decrease stripping materials and save money, it also increases the risk associated with slope surges. Therefore, optimising slopes is crucial for both financial and safety reasons. Numerical models such as the finite element method experience challenges in mesh generation of heterogeneous systems characterised by varying material properties and stratigraphies. Moreover, the need for repetitive geometry update necessitates recursive mesh regeneration that increases the computational burden. Moreover, previous slope optimisation studies focus solely on dry conditions. To consider the complex condition of hydrology along with heterogeneity in the soil stratigraphy, this study develops an optimisation procedure by combining the particle swarm optimisation algorithm and the scaled boundary finite element with an image-based meshing technique to optimise slopes with groundwater and achieve the desired factor of safety (FoS). The method changes the slope design parameters and the phreatic surface of groundwater simultaneously, considering user-defined parameters while iteratively re-meshing the optimisation processes. Several cases are presented, demonstrating the optimisation of bench width, bench angle, backfill parameters, and groundwater pumping levels.

1. Introduction

Recent growth in the manufacturing industry has increased the demand for raw materials to meet production needs. As a result, many open-pit mines have transitioned into deep mines to enhance mineral extraction. With this shift comes a significant challenge: slope instability. As the mines deepen, the risk of slope instability increases, which could have severe consequences for the safety of miners, the economy, and the environment.

One of the main goals of mining projects is to generate significant economic returns. Several methods can be employed to achieve this. These include minimising overburden removal, enhancing the stripping ratio, and targeting high-grade mining blocks [1]. These techniques are often utilised during the extraction and planning phases of mining to maximise profits. However, such applications are constrained by certain limitations that impact their effectiveness. For example, weak shear strength parameters of geomaterials and ground water existency limit the improvement of stripping ratio and targeting high grade zones is always not possible.

The overall slope angle is a crucial factor that can significantly affect the operational costs of a mining site. Even minor improvements in the slope angle can lead to a substantial reduction in overburden stripping costs and a significant increase in ore recovery [2]. However, it is important to keep in mind that there is also an increased risk associated with such changes. Irrespective of economic gains, the primary concern of slope design is safety and stability. Therefore, consideration of economic together with safety factors and designing the optimum slope is vital in any mining operation.

A variety of techniques have been developed to analyse the stability of slopes. These methods can be broken down into two main categories:

* Corresponding author.
E-mail address: e.ooi@federation.edu.au (E.T. Ooi).

https://doi.org/10.1016/j.enganabound.2024.105976
Received 24 June 2024; Received in revised form 18 September 2024; Accepted 19 September 2024
Available online 27 September 2024

limit equilibrium methods (LEM) and numerical methods. Examples of LEM include Bishop's method [3] and Spencer's method [4], whereas numerical methods include finite difference method (FDM) [5], finite element method (FEM) [6], and scaled boundary finite element method (SBFEM) [7].

In early approaches, LEMs were extensively utilised for their ease of application and for providing a fair approximation of slope stability. However, due to their limitation of only being applicable to predetermined slip surfaces, the identification of the critical surface is not a straightforward process. As a result, optimisation algorithms are employed with LEMs to find the minimum factor of safety (FoS) and the corresponding slip surface [8,9]. In addition, optimisation techniques along with LEM have been used in optimising the slope geometry. The popular optimisation techniques include particle swarm optimisation (PSO) [10], genetic algorithm (GA) [11] and ant colony optimisation (ACO) [12].

Similar classes of problems have also been attempted using a combination of numerical methods and optimisation techniques. For instance, Wijesinghe et al. [13] utilised the scaled boundary finite element method (SBFEM) together with genetic algorithm to optimise slope geometries. Wang et al. [14] applied FEM techniques to optimise the geometry of a retaining wall required for slope stability. Jurgens and Henke [15] combined the FEM, the PSO and the differential evolution method to optimise pit excavation process. Napa-García et al. [16] applied the conjugated gradient method along with FLAC3D to optimise room and pillar dimensions in a building.

The studies aforementioned considered only the impact of dry conditions when optimising the geotechnical structure. Nevertheless, it is important to note that groundwater is present within the geotechnical system most of the time in real-life conditions. Therefore, it is crucial to consider the presence of groundwater in the analysis. Incorporating the phreatic surface into the geotechnical modelling increases the complexity of the required analysis. As optimisation is an iterative process, numerical methods such as FEM face challenges in automating the updating of geotechnical structure parameters and meshing/remeshing necessitating significant human interaction.

To address the challenges associated with slope parameter optimisation, we developed an SBFEM-based optimisation method that incorporates an image-based meshing technique. This approach enables the integration of static groundwater within the model. Mesh generation and regeneration are fully automatic and are carried out using digital images of slopes that are progressively updated using the optimisation process. This also allows for easy integration of static groundwater profile alterations based on the slope geometry. The image-based meshing technique significantly minimise human involvement in the numerical simulation.

This paper is divided into several sections, including a discussion on the scaled boundary formulation for the elastoplastic model under static conditions, overview of the image-based mesh generation used in this study and implementation of particle swarm optimisation techniques in Section 2, an analysis of five examples that demonstrate the proposed approach's capabilities in Section 3, and discussion and conclusion in Section 4. The examples focus on optimising bench width, bench angle, backfill height and width, while considering the phreatic groundwater surface.

2. Scaled boundary formulation

2.1. Governing equations for poro-elasto-plastic media

In this study, the slope is assumed to be of a poro-elasto-plastic material. The static fluid in the geology is assumed to represent the ground water imbalance. Hence, the linear static balance for pore pressure and the solid can be expressed as

$$\mathbf{L}_u^T \boldsymbol{\sigma} + \rho \mathbf{g} = \mathbf{0} \tag{1}$$

The total stress $\boldsymbol{\sigma}$ can be expressed in terms of effective stress $\boldsymbol{\sigma}'$ and the pore fluid pressure, p as

$$\boldsymbol{\sigma} = \boldsymbol{\sigma}' - \alpha \mathbf{m} p \tag{2}$$

where $\boldsymbol{\sigma}' = \mathbf{D}\boldsymbol{\epsilon}$, α is Biot's constant and $\mathbf{m} = \begin{bmatrix} 1 & 1 & 0 \end{bmatrix}^T$. Here, $\mathbf{g}$ is the gravitational acceleration, $\mathbf{D}$ is the elastic constitutive matrix and $\boldsymbol{\epsilon}$ is the strain. We note here that the elasto-plasticity is modelled using the initial stiffness approach. $\mathbf{L}_u$ is a linear differential operator defined as

$$\mathbf{L}_u = \begin{bmatrix} \frac{\partial}{\partial x} & & \frac{\partial}{\partial y} \\ & \frac{\partial}{\partial y} & \frac{\partial}{\partial x} \end{bmatrix}^T \tag{3a}$$

Using the method of weight residuals, the weak form of Eq. (1) is expressed as

$$\int_\Omega \delta\boldsymbol{\epsilon}^T \Delta\boldsymbol{\sigma}' d\Omega = \int_\Gamma \delta\mathbf{u}^T \Delta\mathbf{t} d\Gamma + \rho \int_\Omega \delta\mathbf{u}^T \mathbf{g} d\Omega - \int_\Omega \delta\boldsymbol{\epsilon}^T (\boldsymbol{\sigma}' + \alpha\mathbf{m}p) d\Omega \tag{4}$$

Here, we decompose the total stress as

$$\boldsymbol{\sigma} = \boldsymbol{\sigma}' + \Delta\boldsymbol{\sigma}' - \alpha\mathbf{m}p \tag{5}$$

where the symbol Δ indicates an increment. The pore pressure at each point is assumed to be constant and is calculated from the unit weight of the fluid with reference to a datum. During the analysis, the nodal values of the pore pressure is calculated and interpolated using scaled boundary shape functions for the purpose of integration. $\delta\boldsymbol{\epsilon}$ and $\delta\mathbf{u}$ are the virtual strains and the virtual displacements, respectively. $\mathbf{t}$ is the surface traction on the boundary. We note here that $\Delta\boldsymbol{\sigma} = \Delta\boldsymbol{\sigma}' - \alpha\mathbf{m}\Delta p$ and that $\Delta\boldsymbol{\sigma}' = \mathbf{D}_{ep}\Delta\boldsymbol{\epsilon}$. Eq. (4) is nonlinear and can be solved using numerical methods e.g., FEM and its variants e.g., [6] or meshless methods [17]. In this study, the SBFEM is employed in view of its advantages in

- *Flexible formulation over polygons with an arbitrary number of sides*: The restriction on the geometries that can be adopted for discretisation is significantly relaxed in the SBFEM compared with the FEM. Although the SBFEM is still conditional to star-convex geometries, this requirement can be easily met. This feature makes the SBFEM naturally compliant when quadtree meshes are employed and leads to advantages in computational efficiency [18] and mesh generation.
- *Direct mesh generation from digital images using quadtree mesh*: In 2D, the pixel information in digital images can be employed in mesh generation. A straightforward approach to generate meshes directly from digital images is to assign each pixel as an element in the FEM sense. However, this leads to the requirement of using very fine meshes in the analysis [19]. An alternative approach is to use a quadtree mesh. Finer meshes are used in regions that require more detail e.g., boundaries or interfaces whereas coarser meshes can be used in regions that do not require a detailed discretisation. Application of quadtree meshes, however, introduces hanging nodes that cannot be automatically handled by the FEM unless special constraints or methods are introduced. The SBFEM enables direct use of quadtree meshes leading to an efficient approach for mesh generation with digital images.

2.2. Scaled boundary finite element discretisation

2.2.1. Scaled boundary finite element formulation on polygons/quadtree cells

Fig. 1 shows the representation of the SBFEM coordinate system on a quadtree cell. A cell is composed of a collection of line elements that form a closed loop. In this study only two-node line elements are employed. Along each line element, a local coordinate η is defined similar to that in the FEM. A point denoted here as the scaling centre and having coordinates (x_0, y_0) is defined at the centre of the cell. A

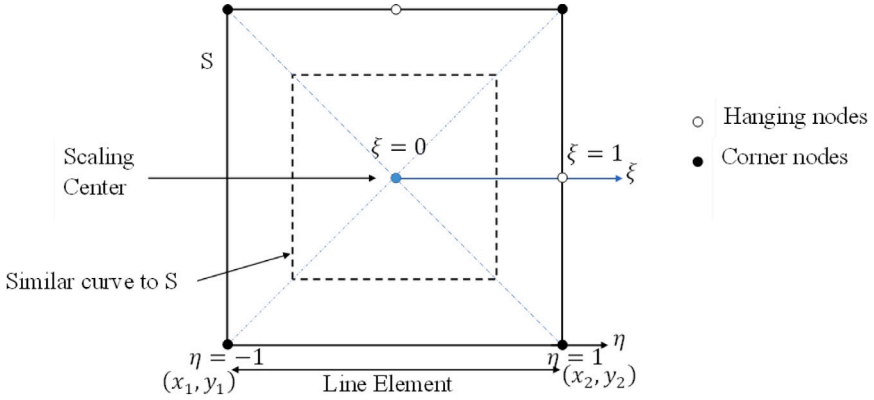

Fig. 1. Scaled boundary coordinate representation on a 6-node quadtree cell.

scaling coordinate ξ is defined such that $\xi = 0$ at the scaling centre and $\xi = 1$ at the boundary.

The Cartesian coordinates (x, y) of a point bounded by the scaling centre and a line element on the cell boundary is expressed as

$$x(\xi,\eta) = x_0 + \xi\overline{\mathbf{N}}_p(\eta)\mathbf{x}_b = x_0 + \xi x_\eta(\eta) \tag{6a}$$

$$y(\xi,\eta) = y_0 + \xi\overline{\mathbf{N}}_p(\eta)\mathbf{y}_b = y_0 + \xi y_\eta(\eta) \tag{6b}$$

where $\mathbf{x}_b$ and $\mathbf{y}_b$ are the nodal $x-$ and $y-$ coordinates of the line element and $\overline{\mathbf{N}}_p(\eta)$ is the shape function matrix of the line element

$$\overline{\mathbf{N}}_p(\eta) = \begin{bmatrix} N_1(\eta) & N_2(\eta) \end{bmatrix} \tag{7}$$

The Cartesian coordinates can also be written in vector form as

$$\begin{Bmatrix} x(\xi,\eta) \\ y(\xi,\eta) \end{Bmatrix} = \begin{Bmatrix} x_0 \\ y_0 \end{Bmatrix} + \xi\overline{\mathbf{N}}_u(\eta)\overline{\mathbf{x}}_b \tag{8}$$

where $\overline{\mathbf{x}}_b$ is the vector of nodal $x-$ and $y-$ coordinates of the line element arranged in Voigt notation and $\overline{\mathbf{N}}_u(\eta)$ is

$$\overline{\mathbf{N}}_u(\eta) = \begin{bmatrix} N_1(\eta)\mathbf{I} & N_2(\eta)\mathbf{I} \end{bmatrix} \tag{9}$$

with a 2×2 identity matrix $\mathbf{I}$.

An infinitesimal line element $d\Gamma$ and infinitesimal area $d\Omega$ is expressed as [20]

$$d\Omega = J(\eta)\xi d\xi \mathrm{d}\eta \tag{10}$$

$$d\Gamma = \xi\sqrt{(x_{\eta,\eta}(\eta))^2 + (y_{\eta,\eta}(\eta))^2}d\eta = \xi L(\eta)d\eta \tag{11}$$

where $J(\eta)$ is the determinant of the Jacobian matrix, given by:

$$\mathbf{J}(\eta) = \begin{bmatrix} x_\eta(\eta) & y_\eta(\eta) \\ x_{\eta,\eta}(\eta) & y_{\eta,\eta}(\eta) \end{bmatrix} \tag{12}$$

2.2.2. Scaled boundary finite element shape functions

To discretise Eq. (4), scaled boundary shape functions Ooi et al. [21] are employed. The virtual displacements $\delta\mathbf{u}$; and the $\Delta\mathbf{u}$ expressed as

$$\delta\mathbf{u}(\xi,\eta) = \mathbf{N}_u(\xi,\eta)\delta\mathbf{u}_b \tag{13a}$$

$$\Delta\mathbf{u}(\xi,\eta) = \mathbf{N}_u(\xi,\eta)\Delta\mathbf{u}_b \tag{13b}$$

where $\mathbf{N}_u(\xi,\eta)$ are the shape function matrices for displacement field, respectively. $\Delta\mathbf{u}_b$ is the incremental nodal displacements and $\delta\mathbf{u}_b$ is an arbitrary vector representing the virtual displacements. The shape functions are

$$\mathbf{N}_u(\xi,\eta) = \overline{\mathbf{N}}_u(\eta)\mathbf{V}_u^{(e)}\xi^{-\mathbf{\Lambda}_u}\mathbf{V}_u^{-1} \tag{14}$$

where $\mathbf{\Lambda}_u$ is a diagonal matrix containing the eigenvalues obtained from the solution of the equilibrium equation. $\mathbf{V}_u$ is a square matrix containing the eigenvectors corresponding to $\mathbf{\Lambda}_u$. We do not aim to derive the solution for $\mathbf{\Lambda}_u$ and $\mathbf{V}_u$; and direct instead the reader to standard SBFEM literature e.g., Song [20], Ooi et al. [21]. The superscript $*^{(e)}$ indicates that only the rows of $\mathbf{V}_u$ corresponding to the degrees-of-freedom of a line element on the cell boundary are used in the calculation.

The incremental (and virtual) strains are obtained by applying the linear differential operators $\mathbf{L}_u$ to $\Delta\mathbf{u}$ and $\delta\mathbf{u}$ leading to

$$\Delta\boldsymbol{\epsilon}(\xi,\eta) = \mathbf{L}_u\Delta\mathbf{u}(\xi,\eta) = \mathbf{B}_u(\xi,\eta)\Delta\mathbf{u}_b \tag{15a}$$

$$\delta\boldsymbol{\epsilon}(\xi,\eta) = \mathbf{L}_u\delta\mathbf{u}(\xi,\eta) = \mathbf{B}_u(\xi,\eta)\delta\mathbf{u}_b \tag{15b}$$

Here, $\mathbf{B}_u(\xi,\eta)$ is the strain–displacement matrix calculated as

$$\mathbf{B}_u(\xi,\eta) = \mathbf{\Psi}_u(\eta)\xi^{-\mathbf{\Lambda}_u-\mathbf{I}}\mathbf{V}_u^{-1} \tag{16}$$

where

$$\mathbf{\Psi}_u(\eta) = J^{-1}(\eta)\left(-\begin{bmatrix} y_{\eta,\eta}(\eta) & \\ & -x_{\eta,\eta}(\eta) \\ -x_{\eta,\eta}(\eta) & y_{\eta,\eta}(\eta) \end{bmatrix}\overline{\mathbf{N}}_u(\eta)\mathbf{V}_u^{(e)}\mathbf{\Lambda}_u + \begin{bmatrix} -y_\eta(\eta) & \\ & x_\eta(\eta) \\ x_\eta(\eta) & -y_\eta(\eta) \end{bmatrix}\overline{\mathbf{N}}_{u,\eta}(\eta)\mathbf{V}_u^{(e)}\right) \tag{17}$$

The pore pressure in Eq. (4) is interpolated from the nodal values $\mathbf{p}_b$ as

$$p(\xi,\eta) = \mathbf{N}_p(\xi,\eta)\mathbf{p}_b \tag{18}$$

where the shape function $\mathbf{N}_p(\xi,\eta)$ is Song [20], Ooi et al. [21]

$$\mathbf{N}_p(\xi,\eta) = \overline{\mathbf{N}}_p(\eta)\mathbf{V}_p^{(e)}\xi^{-\mathbf{\Lambda}_p}\mathbf{V}_p^{-1} \tag{19}$$

where $\mathbf{\Lambda}_p$ is a diagonal matrix containing the eigenvalues obtained from the solution of the Laplace equation. $\mathbf{V}_p$ contains the eigenvectors corresponding to $\mathbf{\Lambda}_p$ and $\overline{\mathbf{N}}_p(\eta) = \begin{bmatrix} N_1(\eta) & N_2(\eta) \end{bmatrix}$.

2.2.3. Discretisation of governing equations

Substituting Eqs. (13b) and (15b) into Eq. (4) results in

$$\int_\Omega \mathbf{B}_u^T\mathbf{D}\mathbf{B}_u d\Omega\Delta\mathbf{u}_b = \int_\Gamma \mathbf{N}_u^T\Delta\bar{\mathbf{t}}d\Gamma + \int_\Omega \mathbf{N}_u^T\rho\mathbf{g}d\Omega - \left(\int_\Omega \mathbf{B}_u^T\boldsymbol{\sigma}'d\Omega - \int_\Omega \mathbf{B}_u^T\alpha\mathbf{m}\mathbf{N}_p d\Omega\mathbf{p}_b\right) \tag{20}$$

where the dependence of the shape functions and derivatives on (ξ,η) have been removed for brevity. Eq. (20) can be simplified as

$$\mathbf{K}\Delta\mathbf{u}_b = \mathbf{F}_u - \mathbf{R}_u \tag{21}$$

with

$$\mathbf{K} = \int_\Omega \mathbf{B}_u^T\mathbf{C}_u\mathbf{B}_u d\Omega \tag{22a}$$

$$\mathbf{F}_u = \int_\Gamma \mathbf{N}_u^T\Delta\bar{\mathbf{t}}d\Gamma + \int_\Omega \mathbf{N}_u^T\rho\mathbf{g}d\Omega \tag{22b}$$

$$\mathbf{R}_u = \int_\Omega \mathbf{B}_u^T\boldsymbol{\sigma}'d\Omega - \int_\Omega \mathbf{B}_u^T\alpha\mathbf{m}\mathbf{N}_p d\Omega\mathbf{p}_b \tag{22c}$$

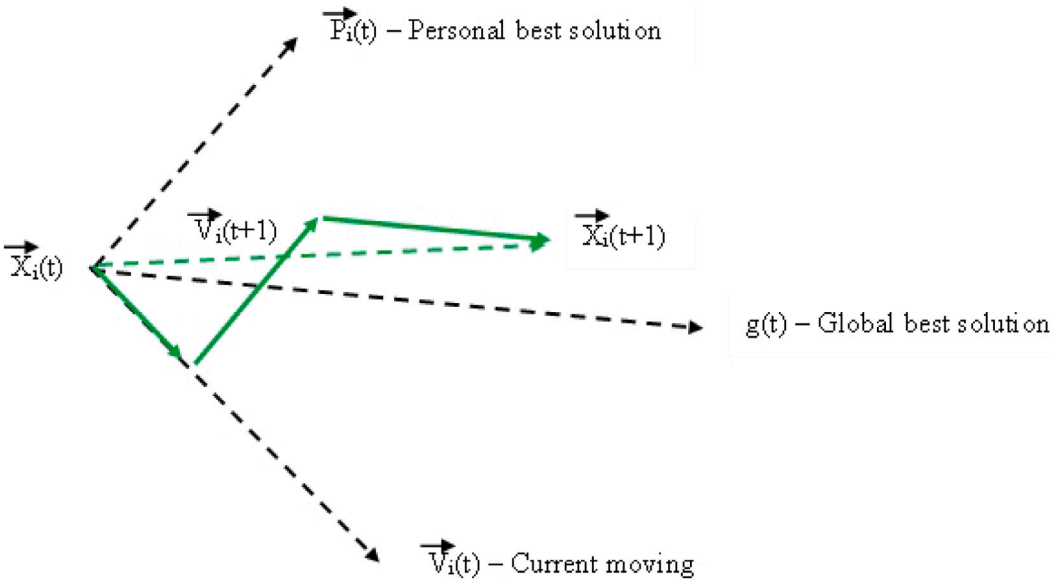

Fig. 2. Movement of a particle according to PSO.

Eqs. (22a) and (22c) can be integrated using standard approaches adopted in the SBFEM. We detail the integration of the coefficient matrix and vectors in Appendix.

The Mohr–Coulomb yield criteria is considered as failure criteria in this study. The return mapping algorithm [22] is implemented to return the stresses at the gauss points to the surface f

$$f = \left(\sqrt{3}\cos\gamma_0 - \sin\gamma_0\sin\phi\right) q - 3p\sin\phi - 3c\cos\phi = 0 \tag{23}$$

where p, q and γ_0 are stress invariants while ϕ and c are friction angle and cohesion, respectively. In this study, the convergence tolerance value and the iteration ceiling limit of 1×10^{-4} and 500, respectively, are considered. The model can handle associative $\left(\frac{\partial f}{\partial \phi}\right)$ and non associative $\left(\frac{\partial f}{\partial \psi}\right)$ plastic potential, where ψ is the dilation angle.

2.2.4. Shear strength reduction technique

In this study, the Factor of Safety (FoS) of slopes is used as a constraint in the slope design. The shear strength reduction technique [6] is adopted for this purpose. For the Mohr–Coulomb failure adopted in this study, the soil shear strength is [3]

$$\tau = c_0 + (\sigma - p)\tan\phi_0 \tag{24}$$

where τ is shear strength, c_0 is initial cohesion, ϕ_0 is initial friction angle, p is pore pressure, and σ is total stress (compression designated as positive).

The shear strength reduction method iteratively reduces the cohesion and friction angle by a strength reduction (SRF) according to

$$c = \frac{c_0}{\mathrm{SRF}} \tag{25}$$

$$\phi = \tan^{-1}\frac{\tan\phi_0}{\mathrm{SRF}} \tag{26}$$

Here c and ϕ are the reduced effective cohesion and effective friction angle, respectively. The SRF is progressively increased in steps of 0.01 until non-convergence of the poro-elasto-plastic analysis is observed [7]. During this process, while the pore pressure is constrained at a constant value, ensuring fully drained conditions [23]. During each time step where the FoS is required to be calculated, the stress, strains and pore pressure are taken as the initial condition for the FoS calculation. The FoS is then calculated from the SRF during the consolidation as an independent process.

2.3. Particle swarm optimisation of slope geometry with scaled boundary finite element method

2.3.1. Particle Swarm Optimisation (PSO)

Particle swarm optimisation (PSO) [10] is a population-based search algorithm. Each candidate solution in the population is termed a particle. Each particle has its own personal best solution whereby its motion defined by a position and a velocity is tracked within the search space through simple mathematical formula. The population as a whole has a global best solution that is derived from the motion of all the particles in the search space. Improvements of a trial solution is achieved iteratively within a search-space.

Particles in motion are inclined to move together until they lose their momentum. The particle's movement is a result of its own experience and that of its neighbours. Two essential components determine the particle's movement i.e., personal best solution and global best solution. The particle's personal best solution (pbest) indicates the best position it has achieved so far, while the global best solution (gbest) denotes the best position among all particles in the swarm.

The velocity and position of each particle undergo iterative updates utilising the following formulas:

$$X_{ij}(t+1) = X_{ij}(t) + V_{ij}(t+1) \tag{27}$$

$$V_{ij}(t+1) = W.V_{ij}(t) + r_1.C_1\left[P_{ij}(t) - X_{ij}(t)\right] + r_2.C_2\left[g_j(t) - X_{ij}(t)\right] \tag{28}$$

where, $W.V_{ij}(t)$ is inertia term, $r_1.C_1\left[P_{ij}(t) - X_{ij}(t)\right]$ is cognitive component and $r_2.C_2\left[g_j(t) - X_{ij}(t)\right]$ is social component while W is inertia coefficient, i is velocity of particle, j is component of velocity, t is number of iteration, r_1 and r_2 are random numbers and C_1 and C_2 are acceleration coefficients. Both pbest and gbest solutions are improved iteratively until the pbest and gbest converges into an optimal solution, which is commonly known as the Particle Swarm Optimisation as shown in Fig. 2.

2.3.2. A PSO-SBFEM algorithm for optimisation of open pit slopes

In open pit slopes, design parameters such as the bench angle, the bench width, the backfill height and the backfill width (as shown in Fig. 3) affect their stability. Depending on the application, various optimisation problems of slope design parameters can be constructed.

The PSO is applied in tandem with the SBFEM to optimise these design parameters as is shown in Fig. 4. The SBFEM carries out the

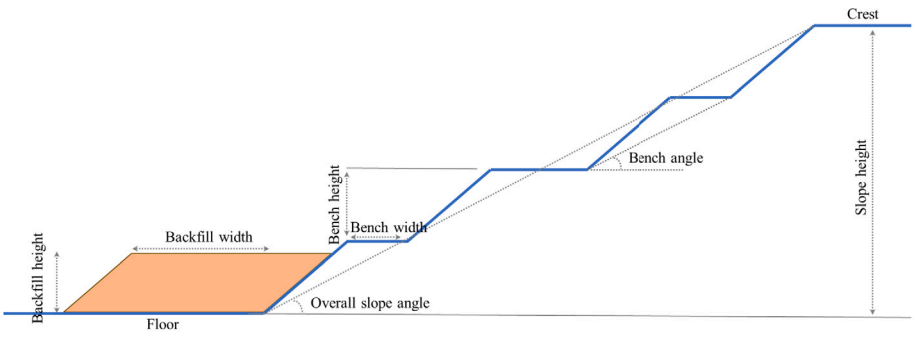

Fig. 3. Slope geometry.

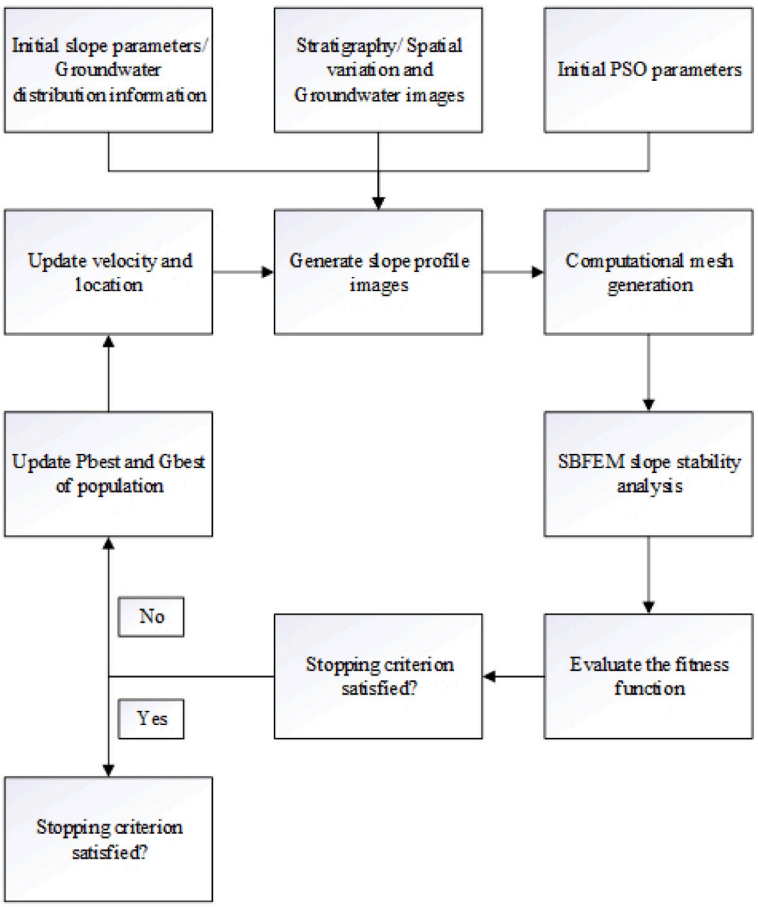

Fig. 4. PSO slope design parameters optimisation flow chart.

slope stability analysis based on the target FoS. The resulting open pit slope design is used to inform the PSO if a further optimisation of the slope geometry is required.

To start the analysis, the algorithm require as inputs digital images representing the information of the soil stratigraphy (and material property variation if any), the phreatic surface and the initial slope geometry. The slope geometry can be defined using simple mathematical operators as a function of the slope design parameters e.g., number of benches, bench width and bench angle that need to be optimised. For the optimisation algorithm, the upper and lower bounds of the slope design parameters, the size of the initial population, the number of iterations are required as input. The required FoS, which is an additional constraint in the optimisation problem is also prescribed during this step.

The digital images are then used to generate the computational mesh. The quadtree decomposition is employed given its compatibility with the SBFEM and ability to directly generate a mesh from digital images. Some considerations were made when generating the phreatic surface to compensate for instances where the domain of the water body is located outside of the soil. We describe these in Section 2.3.3. Section 2.3.4 outlines the mesh generation process.

A poro-elasto-plastic analysis is then carried out to identify the FoS of the current slope geometry. The fitness function of the PSO is then computed. The computations will exit when an optimal solution subject

(a) Bench angle θ greater than phreatic angle α (b) Bench angle θ less than phreatic angle α

Fig. 5. Phreatic angle consideration with bench angle.

to the prescribed constraints is obtained. Otherwise, current solution is used to update the pbest and gbest solution the population. This result also defines the updated geometry of the slope in the digital images for the next analysis. The process then repeats until an optimal solution is finally obtained.

In this study, the maximum number of iterations is set as the stopping criterion. The number of iterations is set to 25 and the total number of population used for the optimisation is 15. The fitness function is determined by considering the slope angle as a whole when optimising slope parameters, or the backfill area when optimising backfill parameters, or the pumping depth when optimising pumping depth. If a failure occurs during the iteration, a penalty value is factored in to the fitness function, causing the value for that iteration to deviate from the optimum value. In this study, the weight constants for the current search direction, local best search direction, and global best search direction were 0.5, 1, and 1, respectively.

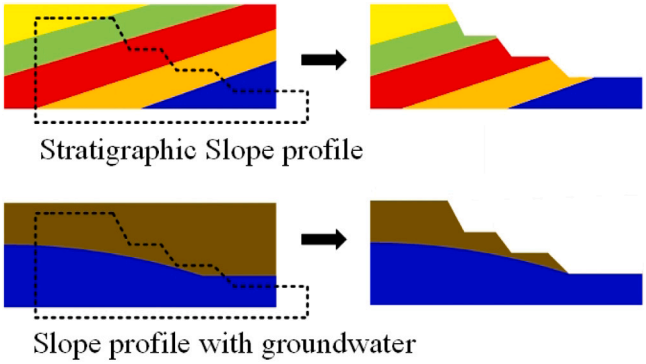

Fig. 6. Automatic image-based slope profile generation.

2.3.3. Automatic slope profile generation

The PSO is adopted in this study to optimise the design parameters of a slope such as bench angle, bench width, backfill height and backfill width. The existing slope geometric parameters or initial parameters such as bench width, bench height, number of benches and phreatic line are introduced into PSO along with the PSO initial parameters.

The groundwater profile image is generated according to the phreatic line. Generation of the phreatic surface depends on the bench angle and falls under two cases i.e., (a) Bench angle θ greater than phreatic angle α and (b) Bench angle θ less than phreatic angle α as shown in Fig. 5. When $\theta > \alpha$, the phreatic line is located entirely within the slope. The digital image generated from the phreatic surface can be used directly for mesh generation. When $\theta < \alpha$, the phreatic surface angle adjusted to bench angle as shown in Fig. 5 and a constant gradient is assumed from the toe of the bench to the next.

These conditions are considered during automatic slope profile generations. We note here that different profiles of the groundwater can be defined by making use of the two principles in the above. If required, the depth of the phreatic line or the angle of the phreatic line can also be used as input as in an optimisation problem.

2.3.4. Image-based quadtree mesh generation

During optimisation, the geometry of the slope (and groundwater profile) change during each iteration and necessitates repetitive mesh generation. To facilitate automation of mesh generation, digital images are employed. Because the analysis considers the coupled behaviour between the solid and the pore fluid pressure two digital images are required as input. The first image informs the stratigraphy of the slope. The second image informs the groundwater profile.

The digital images are initially of size $M \times N$ pixels. In the image that contains the stratigraphy information, the colour code in each pixel is used to identify the different material types in the slope. In the image that contains the groundwater profile information, only two colours are required to distinguish between wet and dry regions.

For a given slope geometry (irrespective of whether it is an initial condition or an interim output during the optimisation process), the outer boundary of the slope is completely defined by the bench width, the bench height, the number of benches. During optimisation, information on these variables are continuously updated. After each iteration, the outer boundary is then overlapped on the images containing the stratigraphic and groundwater profiles as shown in Fig. 6. The images are then trimmed to generate two separate images defined by the boundary of the slope. To facilitate rapid mesh generation from digital images, quadtree decomposition is employed.

Quadtree decomposition is a technique used to divide a two-dimensional space into four quadrants or children. It is an iterative method used to partition regions based on numerical values. In the initial decomposition, the original image divides into four quadrants, and each quadrant is divided into another four quadrants in subsequent iterations. This process continues until a single quadrant contains data with the same numerical value.

When adopting quadtree decomposition, it is important to consider the size of the quadrants in the final mesh. The mesh resolution is usually determined by the fine details in the stratigraphy or the groundwater profile. The smallest size of a quadtree cell in this study is adjusted so that it is sufficient to represent the stratigraphy and the ground water profile at a desired accuracy.

The image-based quadtree mesh generation is fully computer-driven, reducing the need for human involvement during mesh generation. The relevant data can be fed as digital images to a computer. The quadtree decomposition can easily be implemented using MATLAB R2020 inbuilt function ‘qtdecomp’.

To generate the mesh, separate digital images containing information on the stratigraphy, spatial variation of material properties and groundwater distribution, respectively are used as inputs. The mesh generation method proposed by Wijesinghe et al. [7] is augmented for use in this study to consider the ground water profile. All images are considered simultaneously in the quadtree decomposition.

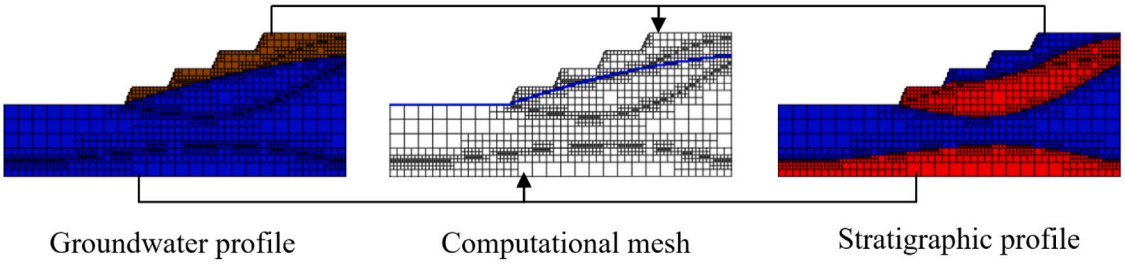

Fig. 7. Computational mesh generation combining, Stratigraphy and groundwater distribution images.

Table 1
Geomaterial parameters.

	Represent colour	Elastic modulus (kPa)	Poisson's ratio	Cohesion (kPa)	Friction Angle (°)	Saturated weight (kN/m3)	Unsaturated weight (kN/m3)
Coal	Red	40 000	0.2	150.72	27.28	11.5	11
Soil	Blue	52 000	0.3	31.81	23.67	20.2	20

Table 2
Optimised bench widths for phreatic parameter changes.

(a) $d = 10$ m			
α	x(m)	$\bar{\theta}$	No. Iterations
19°	8.8	41.6°	496
20°	9.3	40.6°	495
21°	10.4	38.7°	489
22°	11.5	37.0°	499
(b) $d = 13$ m			
α	x(m)	$\bar{\theta}$	No. Iterations
19°	8.8	41.6°	490
20°	9.2	40.8°	492
21°	10.1	39.2°	488
22°	11.0	37.8°	496

The colour information of the pixels in the digital image containing the stratigraphy (and/or material parameters) are assigned to corresponding quadtree cells, as shown in Fig. 7. The image containing groundwater profile is used to identify the cells below the phreatic line. Only two colours are required to distinguish between wet and dry regions. In this study, the groundwater profile is assumed to be static during the entire poro-elasto-plastic analysis. The quadtree is particularly appropriate to generate meshes of this kind as it is able to effectively bridge the transition between regions of finer to coarser element sizes in the mesh due to changes in the stratigraphy and groundwater profile within the domain [7].

3. Numerical examples

In this section, four examples are illustrated to demonstrate the optimisation ability of different slope geometries, considering the effect of groundwater and phreatic surface variation along the slope geometry variation. The considered examples are

I Slope angle and bench width optimisation considering constant phreatic surface in a simplified slope
II Bench width optimisation in simplified slope considering phreatic surface changes along with the overall slope angle
III Backfilling optimisation at the slope toe to enhance the FoS while considering the inclined phreatic surface within the backfilling.
IV Pumping the water to lower the phreatic surface and enhance the FoS of slope.

The convergence tolerance value and the iteration ceiling value for the elastoplastic model are 0.0001 and 500, respectively. This study presents the slope geometries to an accuracy of 0.1 m. The right and left edges of the mesh are constrained for horizontal displacement, while the bottom edge is fixed during the elastoplastic analysis.

3.1. Bench width optimisation

In this example, bench width x of a 3-bench open pit slope is optimised under the condition of static groundwater. All other parameters of the slope are considered to be constant. The stratigraphy is defined by horizontal layers of coal and soil. The material parameters of the coal and soil are given in the Table 1. The digital image of the stratigraphy is of size 512 × 128 pixels as shown in Fig. 8a.

The target FoS value of the slope is 1.5 and an optimal value of x is sought to meet this target value. The water table is considered at d m below the top surface which extends from the bottom of the pit as a curve surface shown in Fig. 8b. The phreatic line is formed considering a circle with radius R for given natural water table angle at toe of the slope. From the geometry, the centre of the circle is calculated and phreatic surface image is generated.

In this example, two values of phreatic surface depth $d = 10$ m and 13 m are considered. The influence of the water table angle is considered in the optimisation by considering the natural phreatic surface gradient at toe of the slope of $19°, 20°, 21°$ and $22°$. The upper boundary and the lower boundary for the bench width optimisation range is 6 m and 16 m respectively. The fitness function considered is:

$$F_{fit} = \frac{1}{Overall\ slope\ angle} + \{No\ Iterations * (Convergency)\} \tag{29}$$

$$where\ Convergency = \begin{cases} 1, & model\ not\ converged \\ 0, & model\ converged \end{cases}$$

Fig. 9 shows the convergence of the global fitness value, X position and velocity variation during the particle swarn optimisation process when $d = 10$ m and $\alpha = 22^0$. Initially, huge changes in the position, velocity and global fitness is observed. After the 12^{th} iteration, subsequent changes are observed to decline. The optimimum value for bench width is reached after 20 iterations. Fig. 10 shows the bench width variation for each iteration in the PSO for the case when $d = 10$ m and $\alpha = 22°$.

The optimised bench widths for different phreatic conditions are shown in Table 2. It is apparent that as the phreatic angle increases, the bench width also increases while the overall slope angle $\bar{\theta}$ decreases.

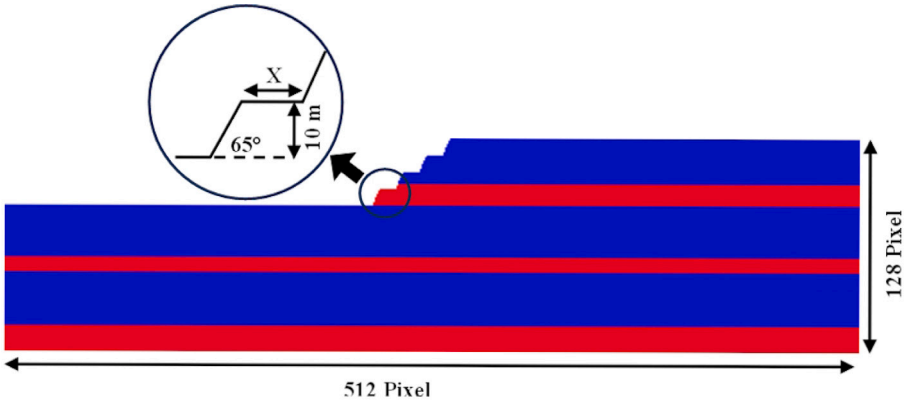

(a) Bench parameters and stratigraphy

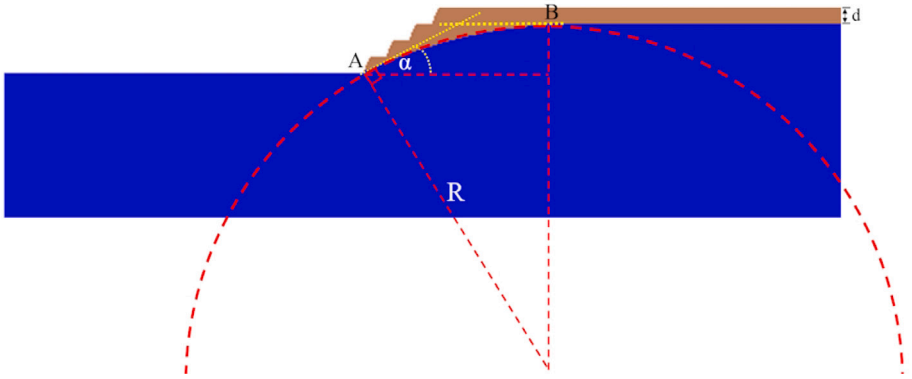

(b) Phreatic surface

Fig. 8. Bench parameters, stratigraphy and phreatic surface.

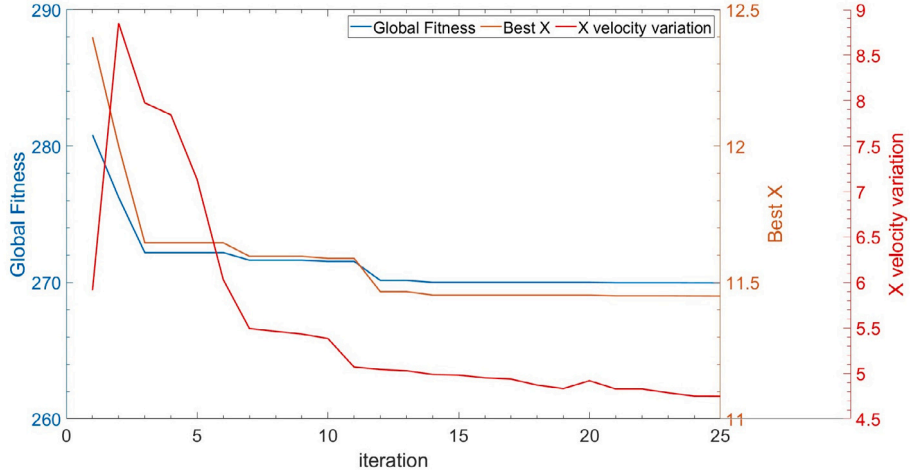

Fig. 9. Global fitness, best X and X variation for all iterations.

The 'overall slope angle' refers to the angle between the highest crest and the lowest toe of a slope.

With the exception of $\alpha = 19°$, a shorter bench width is required to achieve the target FoS when d is increased. It is noted that for the case of $\alpha = 19°$, the optimal bench width is almost similar for both $d = 10\,\text{m}$ and $d = 13\,\text{m}$. This can be explained by the location of the failure surface in either case, which falls above the phreatic surface and there is no effect of pore pressure on slope failure.

To verify the optimised solution, a separate poro-elasto-plastic analysis is conducted using final parameters and material properties scaled

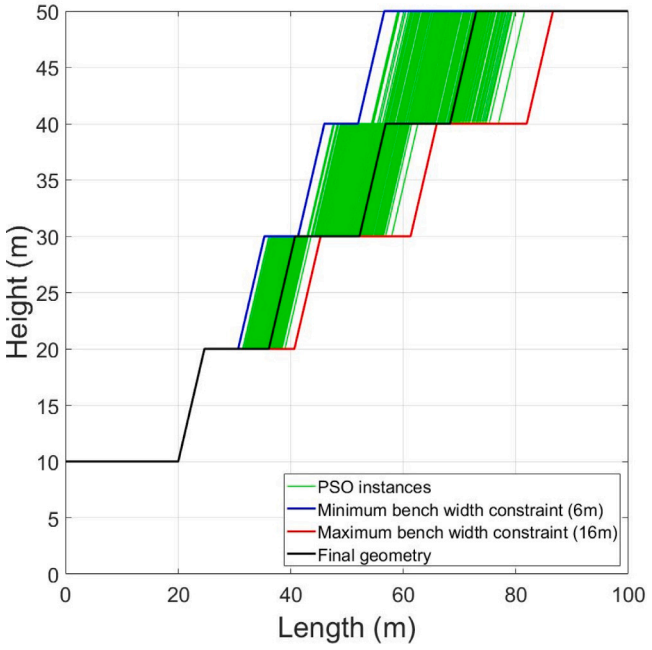

Fig. 10. Bench variation width each iterations.

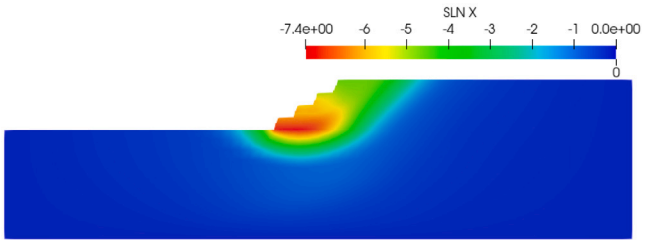

Fig. 11. Deformation of the optimised slope.

by a factor safety value of 1.5. The analysis converged after 499 iterations which is almost equal to the maximum ceiling iteration number. This indicates an observed failure condition at the target factor of safety. The deformation contour map are shown in Fig. 11 clearly outlines the boundary of the failure surface at this state.

3.2. Slope angle and bench width optimisation

This example demonstrates a problem with multi-parameter optimisation on an open pit slope. The bench width (x) and bench angle (θ) of the slope are to be optimised. The material parameters given in Table 1 are considered.

The phreatic surface is considered similar to example 3.1. Two depths of the groundwater profile $d = 10\,\text{m}$ and $d = 13\,\text{m}$ are considered. The optimization problem was undertaken by considering phreatic angles α of $20°, 21°, 22°$ and $24°$ for both values of d. See Fig. 12 for the definition of the parameters and the geoemtry. The target FoS value for all cases is 1.5 and the lower and upper bounds for x and θ are $8\,\text{m} \le x \le 19\,\text{m}$ and $60° \le \theta \le 80°$, respectively. The identical fitness function utilised in Section 3.1 was taken into account in this instance.

Fig. 13 shows the convergence of the global fitness, position and velocity when $d = 10\,\text{m}$ and $\alpha = 20°$ for both x and θ. We note that for other cases, a similar trend is observed. An indication of convergence is observed after 10 iterations. Fig. 14 shows how the bench width and bench angle varies along with each PSO instances.

The optimised bench width and bench angles along with the final overall optimised slope angles are shown in the Table 3. It is clear that

Table 3
Optimised bench width and bench angle for different phreatic angles.

(a) $d = 10$ m				
α	x(m)	θ	$\bar{\theta}$	No. Iterations
20°	11.8	77.5°	42.1°	491
21°	12.4	76.1°	40.3°	494
22°	13.4	77.1°	38.6°	489
24°	17.4	80.0°	34.0°	497
(b) $d = 13$ m				
α	x(m)	θ	$\bar{\theta}$	No. Iterations
20°	10.5	71.5°	41.6°	494
21°	11.8	74.3°	40.6°	492
22°	12.8	75.2°	39.2°	495
24°	15.1	75.2°	35.6°	493

the overall slope angle $\bar{\theta}$ decreases and bench width increases when the phreatic angle at the slope toe increases. This is consistent with physical observations whereby a slope is less stable with increasing water content. This necessitates a stronger structure to achieve the same safety factor as a slope that has less water content.

Increasing the depth of the groundwater profile d is observed to generate a more stable slope. This is evident by the decrease in the bench width and bench angle when $d = 13\,\text{m}$ compared with $d = 10\,\text{m}$. This observation again is related to the water content within the slope.

To confirm the optimised outcome, a distinct elastoplastic analysis is performed by utilising the ultimate optimised parameter and a factor of safety of 1.5. The deformation contour map is depicted in Fig. 15. The final optimised slope reaches a convergence point of 491, which is almost the highest iteration number possible.

3.3. Backfilling optimisation

Backfilling at the toe of a slope is a common precaution taken by engineers to increase the factor of safety of a slope. However, the volume of material required for this process governs the operational costs involve. Hence, identifying the minimum backfilling required helps to avoid unwanted operational costs. This example demonstrate the optimisation of backfilling parameters (backfill width and height) to increase the slope FoS value until a target is reached.

The target FoS value considered is 2.0 and the natural phreatic surface angles of $12°$, $14°$ and $16°$ are considered as different scenarios for the optimisation. The depth of the water table is assumed to be 10 meters below the surface and the rise of the phreatic surface in the backfilling material is taken into account by assuming that a rise in the water table angle starting from the toe of the backfill. The material parameters for coal and soil shown in Table 1 is adopted and the backfilling material parameters are shown in Table 4.

The initial parameters of the slope are shown in Fig. 16a. The backfill angle is considered as to have a gradient of 3H:1V and horizontal backfill width is measured from slope toe to backfill crest. The lower and upper limits are 42 m and 52 m for backfill width while 10 m and 20 m are for backfill height considered. The fitness function used is,

$$F_{fit} = Backfill\ Area + \{No\ Iterations * (Convergency)\} \tag{30}$$

$$where\ Convergency = \begin{cases} 1, & model\ not\ converged \\ 0, & model\ converged \end{cases}$$

Fig. 17 shows the global fitness, backfill height and width variation for each PSO iteration when $d = 10\,\text{m}$ and $\alpha = 12^0$. The best value for the backfill width initially increases while best value for backfill height decreases. Fig. 18 illustrated the backfill profile variation during the optimisation process for each PSO instances.

The optimised backfill geometries and the volume of the material are shown in the Table 5 respect to each phreatic angle. When the

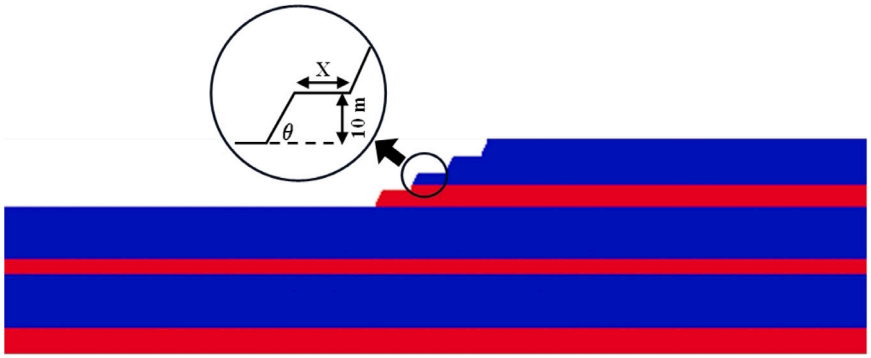

(a) Bench Geometry

(b) Phreatic Surface

Fig. 12. Bench geometry and Phreatic surface.

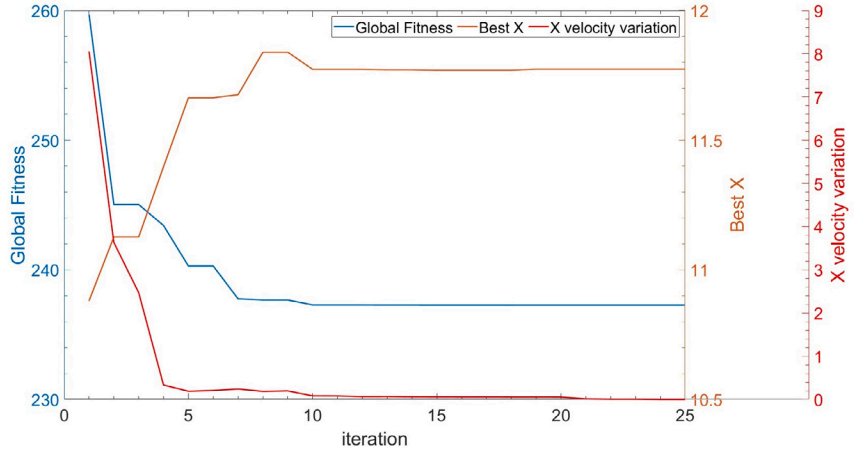

(a) Bench width (x) variation with iterations

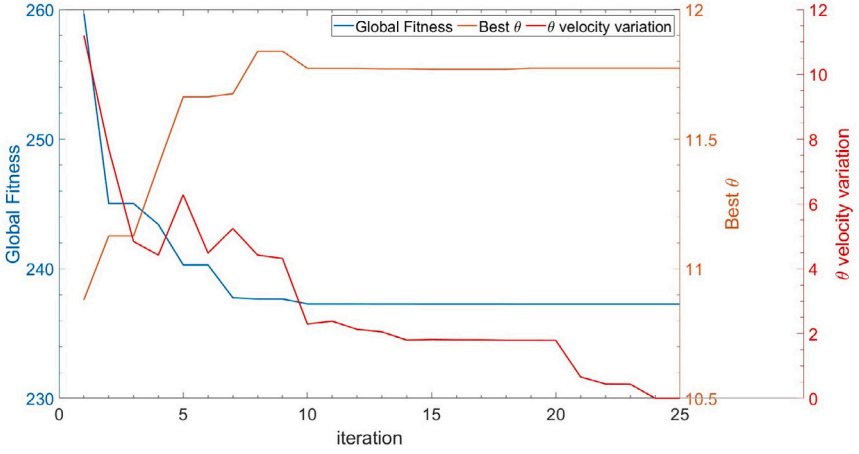

(b) Bench angle (θ) variation with iteration

Fig. 13. Fitness value, best value and velocity value variation with iterations.

Table 4
Backfill material parameters.

	Represent colour	Elastic modulus (kPa)	Poisson's ratio	Cohesion (kPa)	Friction Angle °	Saturated weight (kN/m3)	Unsaturated weight (kN/m3)
Backfill	Yellow	45 000	0.3	40	3	19.5	19

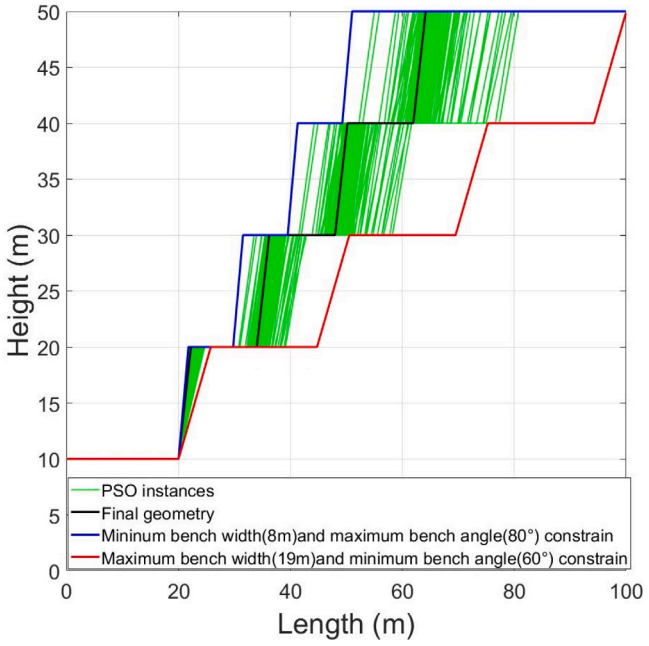

Fig. 14. Bench width and bench angle variation for each iteration.

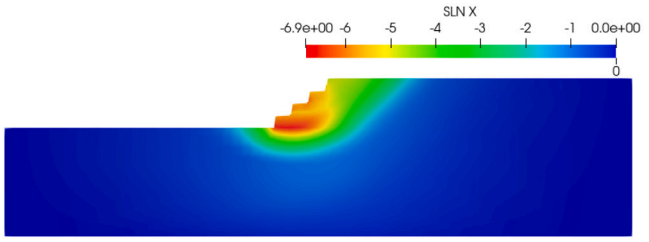

Fig. 15. Deformation contour map for the optimised slope of bench width and bench angle optimisation.

Table 5
Optimised backfill parameters for different phreatic angles.

α	x_1(m)	x_2(m)	Volume of material (m^3)	No. iterations
12°	46.3	12.1	912	497
14°	44.5	15.0	1202	489
16°	42.6	18.0	1528	489

phreatic angle increases, it can have an impact on the stability of a slope. This is because the pore pressure within the slope can increase, causing the strength of the material to decrease. As a result, more backfilling may be required at the toe of the slope. Table 5 provides more information on the specific requirements based on the phreatic angle increase.

To verify the optimised result, a separate elastoplastic analysis is conducted using the optimised parameters and a safety factor of 2. The deformation contour map at the end of the analysis is illustrated in Fig. 19. The ultimate optimised slope achieves a convergence point of 497 which is nearly the maximum iteration value indicating that the optimised parameters achieves the targeted factor of safety.

Table 6
Optimised pumping depths for different phreatic angles at different water table depths.

α	d = 10 m		d = 13 m	
	Pumping depth (m)	No. Iterations	Pumping depth (m)	No. Iterations
20°	20.38	495	15.34	491
21°	22.10	492	19.76	496
22°	24.85	490	22.05	493

3.4. Pumping depth optimisation

Dewatering and lower the phreatic surface is another common technique use to increase the FoS of a slope in open pit mine. However, the extent to which the depth of the phreatic surface is lowered is directly proportional to the cost of pumping and maintenance of the pumps. It is essential to understand the required minimum phreatic surface depth that enhances the FoS to the target value.

To demonstrate such an application, a dewatering pump measured 30 m from the crest of the slope is considered. We assume the groundwater profile to be prismatic around the pumping well. When the phreatic line reaches a steady-state, it is assumed that phreatic surface gradient around the pumping well $\varphi = 30°$. The slope geometries and the phreatic surface around the well is shown in Fig. 20. As depicted in Fig. 20, the water table is situated d meters below the top surface and is represented as a straight line extending from the bottom of the pit. The lower and upper bound limits for the pumping depth is 20 m and 30 m, respectively. The target FoS for the slope is 1.5. The fitness function used is

$$F_{fit} = \frac{1}{Overall\ slope\ angle} + \{No\ Iterations * (Convergency)\} + \{Iteration\ ceiling\ limit - No\ Iterations\} \quad (31)$$

$$where\ Convergency = \begin{cases} 1, & model\ not\ converged \\ 0, & model\ converged \end{cases}$$

Fig. 21 shows the convergence of the global fitness, pumping height variation for each PSO iteration when $d = 10$ m and $\alpha = 22^0$ and Fig. 22 illustrates the phreatic surface variation for difference pumping depths of each PSO instances and the deformation contour map at the end of the analysis is illustrated in Fig. 23.

Table 6 shows the optimal pumping depths for the different values of phreatic angles considered. It is observed that lowering the water table and maintaining a steady level is an effective way to minimise the impact of pore pressure on the strength of materials. The higher the phreatic angle, the deeper the pumping depth required. This observation is related to the increased pore water pressure under a higher phreatic angle. However, when the depth of the phreatic surface from the top surface increases, the corresponding pumping depth for each phreatic angle decreases as the pressure head decreases.

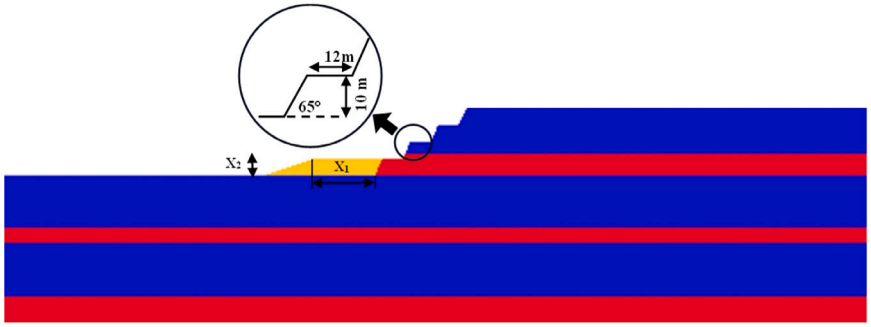

(a) Bench and Backfill geometry

(b) Phreatic Surface

Fig. 16. Backfill and bench parameters and Phreatic surface.

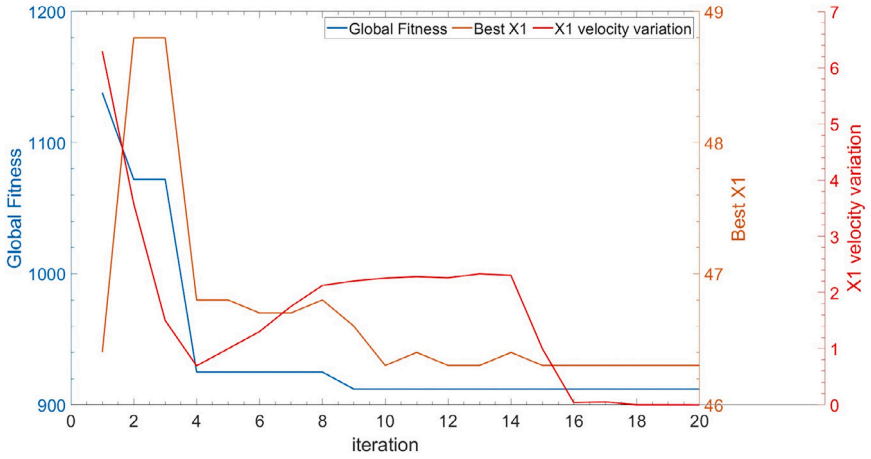

(a) Backfill width variation with iterations

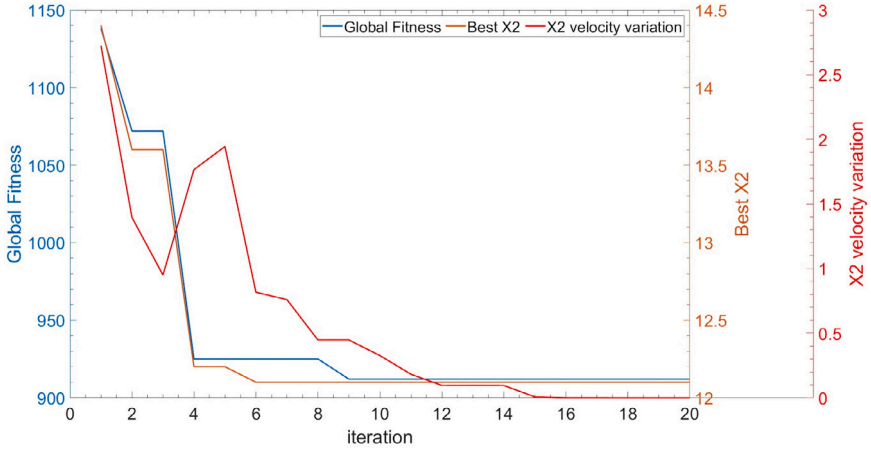

(b) Backfill height variation with iterations

Fig. 17. Fitness, best value and velocities of backfill width and height variation with iterations.

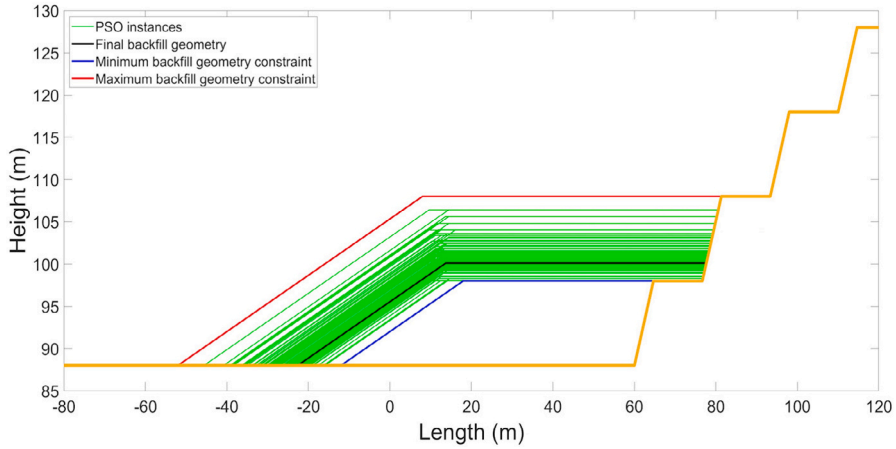

Fig. 18. Backfill width and height variation with each iterations.

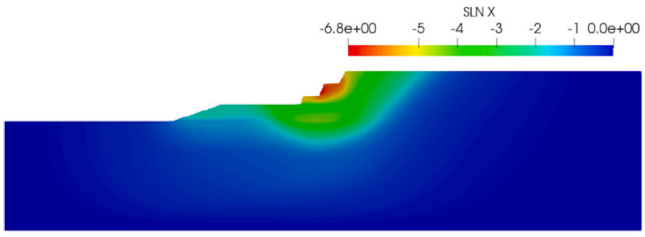

Fig. 19. Deformation contour map for the optimised backfilled geometry.

4. Discussion and conclusion

This paper introduces a numerical framework that aims to optimise slope profiles based on a specified FoS value when ground water is present within the slope. The proposed technique combines several methods, including image-based meshing using quadtree decomposition, elasto-plastic analysis utilising the SBFEM, and slope geometry optimisation using a particle swarm optimisation (PSO). The stability assessment of the slope is conducted based on the Mohr–Coulomb failure criterion.

The use of quadtree decomposition enables fully automatic mesh generation, reducing the need for human interaction in creating the mesh for analysis. This feature proves particularly advantageous in scenarios requiring frequent updates of the computational mesh, as demonstrated in the presented applications. The image-based quadtree meshing technique allows for capturing intricate details and material property distributions based on pixel colour intensity. Consequently, the automation of the PSO optimisation process is facilitated.

The paper showcases four applications of slope geometry optimisation. The first method optimises the bench width for a slope excavation, considering the widths for all benches. The second method optimises both the bench width and angle, maintaining the same values for all benches. The third method focuses on optimising a surcharge backfilling scenario. The fourth application deals with a pumping station and phreatic surface lowering scenario. The optimisation process involves iterations, with the slope geometry evolving at each iteration. Therefore, mesh generation is required at the beginning of each iteration.

Automating the mesh generation process is crucial to facilitate this repetitive optimisation procedure, which can be challenging with other numerical methods like FEM. Including hydrology along with stratigraphy and generating a single mesh capturing both is more complicated, and hence, previous research only focuses on dry conditions. However, the proposed method is capable of generating a mesh considering hydrology variation along with stratigraphy in a single mesh and assigning material parameters to each cell in a fully automatic manner. This reduces computational expenses and human interaction while engaging with optimisation algorithms to optimise the slope geometries when groundwater is present. The presented converged iterations for all final results were very close to the maximum ceiling iteration value, indicating that the results are well optimised. Each optimisation case includes 15 populations and 25 generations, resulting in a total of 375 models. The average optimisation runtime is approximately 12.5 h.

In summary, the image-based SBFEM technique presents several advantages for slope design optimisation. The results emphasise the effectiveness of combining PSO with image-based SBFEM in generating stable and optimised slope geometries with minimal user intervention.

CRediT authorship contribution statement

Dakshith Ruvin Wijesinghe: Writing – original draft, Visualization, Validation, Methodology, Investigation, Formal analysis, Conceptualization. **Ethmadalage Perera:** Validation, Formal analysis. **Ean Hin Ooi:** Writing – review & editing, Software, Conceptualization. **Sundararajan Natarajan:** Writing – review & editing, Software, Conceptualization. **Taghi Sherizadeh:** Writing – review & editing, Supervision, Resources. **Ean Tat Ooi:** Writing – review & editing, Software, Project administration, Methodology, Conceptualization.

Declaration of competing interest

The authors declare that they have no known competing financial interests or personal relationships that could have appeared to influence the work reported in this paper.

Data availability

No data was used for the research described in the article.

Appendix

The integration of the stiffness matrix $\mathbf{K}$ in Eq. (22a) is first considered. Substituting Eqs. (10) and (16) results in

$$\mathbf{K} = \mathbf{V}_u^{-T} \int_{\xi} \xi^{-\boldsymbol{\Lambda}_u - \mathbf{I}} \int_{\eta} \boldsymbol{\Psi}_u^T(\eta) \mathbf{C}_u \boldsymbol{\Psi}_u(\eta) J(\eta) d\eta \xi^{-\boldsymbol{\Lambda}_u} d\xi \mathbf{V}_u^{-1} \tag{A.1}$$

Introducing

$$\mathbf{Y} = \mathbf{V}_u^{-T} \int_{\eta} \boldsymbol{\Psi}_u^T(\eta) \mathbf{C}_u \boldsymbol{\Psi}_u(\eta) J(\eta) d\eta \mathbf{V}_u^{-1} \tag{A.2}$$

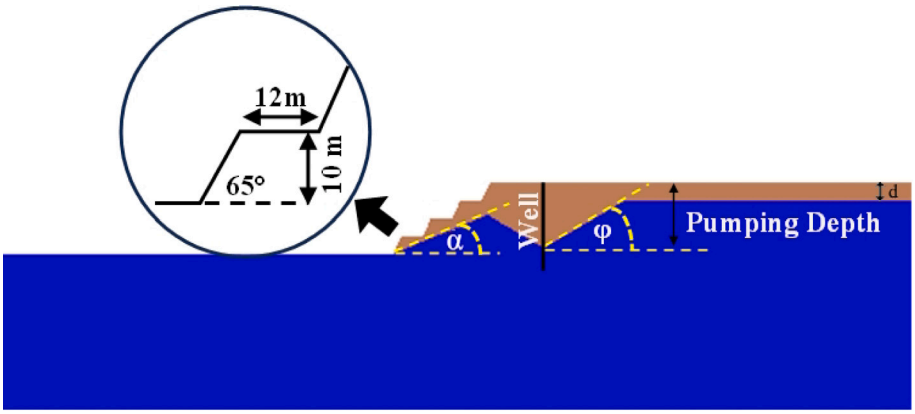

Fig. 20. Geometry of the slope and Phreatic surface around the pumping well.

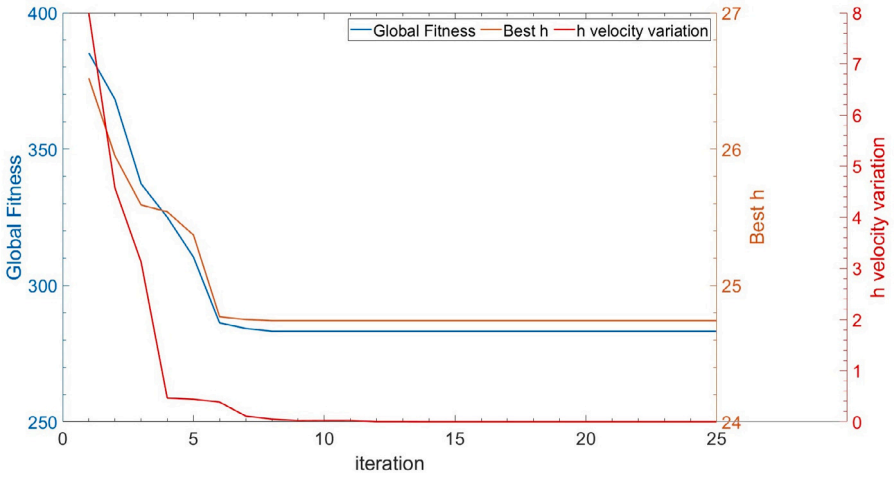

Fig. 21. Fitness, best value and velocities of pumping depth variation with iteration.

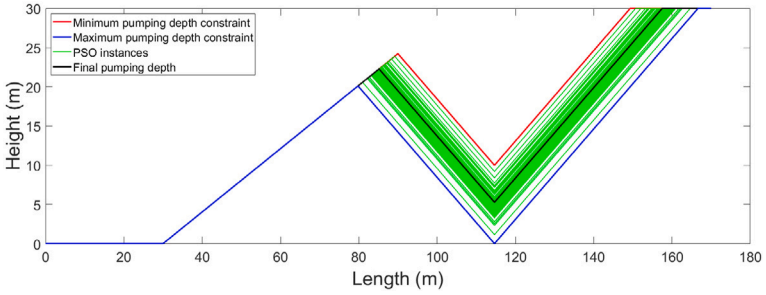

Fig. 22. Phreatic surface variation with pumping depth.

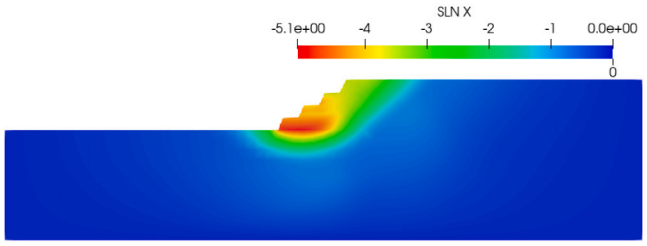

Fig. 23. Deformation contour map for the optimised backfilled geometry.

and making use of the diagonal structure of $\boldsymbol{\Lambda}_u$, each element in the stiffness matrix K_{ij} can be integrated analytically as

$$K_{ij} = \frac{Y_{ij}}{-\lambda_{u_i} - \lambda_{u_j}} \tag{A.3}$$

where Y_{ij} is an element in the matrix $\mathbf{Y}$, λ_{u_i} and λ_{u_j} are the eigenvalues of $\boldsymbol{\Lambda}_u$. The integration of the matrix $\mathbf{Y}$ is performed numerically.

The integration of the external load vector $\mathbf{F}_u$ in Eq. (22b) is considered next. Substituting Eq. (14), Eq. (10) and (11) leads to

$$\mathbf{F}_u = \int_\eta \overline{\mathbf{N}}_u^T(\eta)\Delta\bar{t}L(\eta)d\eta + \rho\mathbf{V}_u^{-T}\int_\xi \xi^{-\boldsymbol{\Lambda}_u+\mathbf{I}}(\mathbf{V}_u^{(e)})^T\int_\eta \overline{\mathbf{N}}_u^T(\eta)\mathbf{g}J(\eta)d\eta d\xi \tag{A.4}$$

We note here that the first term on the right hand side of Eq. (A.4) is a boundary integral evaluated at $\xi = 1$. The term $\mathbf{g}$ in the second term on

the right hand side of Eq. (A.4) is a constant in a slope stability analysis. Integrating analytically results in

$$\mathbf{F}_u = \int_\eta \overline{\mathbf{N}}_u^T(\eta)\Delta\bar{t}L(\eta)d\eta + \rho\mathbf{V}_u^{-T}(-\boldsymbol{\Lambda}_u + 2\mathbf{I})^{-1}(\mathbf{V}_u^{(e)})^T \int_\eta \overline{\mathbf{N}}_u^T(\eta)J(\eta)d\eta\mathbf{g} \quad \text{(A.5)}$$

The integration of the internal load vector $\mathbf{R}_u$ in Eq. (22c) is considered next. Substituting Eqs. (14), (16), (10) and (11)

$$\mathbf{R}_u = \mathbf{V}_u^{-T}\int_\xi \xi^{-\boldsymbol{\Lambda}_u}\int_\eta \boldsymbol{\Psi}_u^T(\eta)\boldsymbol{\sigma}'J(\eta)d\eta d\xi - \alpha\mathbf{V}_u^{-T}\int_\xi \xi^{-\boldsymbol{\Lambda}_u}\int_\eta \boldsymbol{\Psi}_u^T(\eta)\mathbf{m}\overline{\mathbf{N}}_p(\eta)\mathbf{V}_p^{(e)}J(\eta)d\eta\xi^{-\boldsymbol{\Lambda}_p}\mathbf{V}_p^{-1}d\xi\mathbf{p}_b \quad \text{(A.6)}$$

The internal force contribution from the first term of Eq. (A.6) is due to the stress vector $\boldsymbol{\sigma}'$. Representing this term by $\mathbf{R}_\sigma$ and expressing $\boldsymbol{\sigma}'$ as a power function in ξ as

$$\boldsymbol{\sigma}'(\xi,\eta) = \sum_{r=0}\overline{\boldsymbol{\sigma}}_r(\eta)\xi^r \quad \text{(A.7)}$$

leads to

$$\mathbf{R}_\sigma = \mathbf{V}_u^{-T}\sum_{r=0}\int_\xi \xi^{-\boldsymbol{\Lambda}_u+r\mathbf{I}}\int_\eta \boldsymbol{\Psi}_u^T(\eta)\overline{\boldsymbol{\sigma}}_r(\eta)J(\eta)d\eta d\xi \quad \text{(A.8)}$$

Integrating numerically along η and analytically along ξ results in

$$\mathbf{R}_\sigma = \mathbf{V}_u^{-T}\sum_{r=0}(-\boldsymbol{\Lambda}_u + (r+1)\mathbf{I})^{-1}\int_\eta \boldsymbol{\Psi}_u^T(\eta)\overline{\boldsymbol{\sigma}}_r(\eta)J(\eta)d\eta \quad \text{(A.9)}$$

The internal force contribution from the second term of Eq. (A.6) is due to the pore fluid pressure $\mathbf{p}$. Representing this term by $\mathbf{R}_p = \mathbf{C}\mathbf{p}_b$, with the matrix $\mathbf{C}$ expressed as

$$\mathbf{C} = \alpha\mathbf{V}_u^{-T}\int_\xi \xi^{-\boldsymbol{\Lambda}_u}\int_\eta \boldsymbol{\Psi}_u^T(\eta)\mathbf{m}\overline{\mathbf{N}}_p(\eta)\mathbf{V}_p^{(e)}J(\eta)d\eta\xi^{-\boldsymbol{\Lambda}_p}\mathbf{V}_p^{-1}d\xi \quad \text{(A.10)}$$

Introducing

$$\mathbf{X} = \int_\eta \boldsymbol{\Psi}_u^T(\eta)\mathbf{m}\overline{\mathbf{N}}_p(\eta)\mathbf{V}_p^{(e)}J(\eta)d\eta \quad \text{(A.11)}$$

and making use of the diagonal structure of $\boldsymbol{\Lambda}_u$ and $\boldsymbol{\Lambda}_p$, each element in the matrix C_{ij} can be integrated analytically as

$$C_{ij} = \frac{X_{ij}}{-\lambda_{u_i} - \lambda_{p_j} + 1} \quad \text{(A.12)}$$

where λ_{p_j} is an eigenvalue of $\boldsymbol{\Lambda}_p$ and X_{ij} is an element of $\mathbf{X}$.

References

[1] Chaves LS, Carvalho LA, Souza FR, Nader B, Ortiz CEA, Torres VFN, et al. Analysis of the impacts of slope angle variation on slope stability and NPV via two different final pit definition techniques. REM-Int Eng J 2019;73:119–26.

[2] Stacey P. Pit slope design process. In: International symposium on rock slope stability in open pit and civil engineering, Santiago de Chile. 2009.

[3] Bishop AW. The use of the slip circle in the stability analysis of slopes. Geotechnique 1955;5(1):7–17. http://dx.doi.org/10.1680/geot.1955.5.1.7.

[4] Spencer E. A method of analysis of the stability of embankments assuming parallel inter-slice forces. Geotechnique 1967;17(1):11–26. http://dx.doi.org/10.1680/geot.1967.17.1.11.

[5] Lorig L, Varona P. Practical slope-stability analysis using finite-difference codes. In: W. A. Hustrulid M. K. McCarter DJAVZ, editor. Slope stability in surface mining. 2000, p. 115–24.

[6] Griffiths DV, Lane PA. Slope stability analysis by finite elements. Géotechnique 1999;49(3):387–403. http://dx.doi.org/10.1680/geot.1999.49.3.387.

[7] Wijesinghe DR, Dyson AP, You G, Khandelwal M, Song C, Ooi ET. Development of the scaled boundary finite element method for image-based slope stability analysis. Comput Geotech 2022;143:104586. http://dx.doi.org/10.1016/j.compgeo.2021.104586.

[8] Khajehzadeh MRT, Mohammad RT, Mohd ES, Mahdiyeh EA. Locating the general failure surface of earth slope using particle swarm optimisation. Civ Eng Environ Syst 2012;29(1):41–57. http://dx.doi.org/10.1080/10286608.2012.663356.

[9] Mishra M, Maity GVRD. Multiverse optimisation algorithm for capturing the critical slip surface in slope stability analysis. Geotech Geol Eng 2020;38:459–74. http://dx.doi.org/10.1007/s10706-019-01037-2.

[10] Kennedy J, Eberhart R. Particle swarm optimization. In: Proceedings of ICNN'95 - international conference on neural networks. IEEE; 1995, p. 1942–8. http://dx.doi.org/10.1109/icnn.1995.488968.

[11] Holland JH. Adaptation in Natural and Artificial Systems. Ann Arbor, MI, USA: University of Michigan Press; 1975.

[12] Dorigo M. Optimization, learning and natural algorithms. Politecnico di Milano; 1992.

[13] Wijesinghe DR, Dyson AP, You G, Manoj M, Song C, Ooi ET. Simultaneous slope design optimisation and stability assessment using a genetic algorithm and a fully automatic image-based analysis. Int J Numer Anal Methods Geomech 2022;46(15):2868–92. http://dx.doi.org/10.1002/nag.3431.

[14] Wang Y, Smith JV, Nazem M. Optimisation of a slope-stabilisation system combining gabion-faced geogrid-reinforced retaining wall with embedded piles. KSCE J Civ Eng 2021;25(12):4535–51. http://dx.doi.org/10.1007/s12205-021-1300-6.

[15] Jurgens H, Henke S. Numerical optimisation of excavation pit design using finite element analyses. Geotech Geol. Eng. 2023. http://dx.doi.org/10.1007/s10706-023-02639-7.

[16] Napa-García GF, Câmara TR, Navarro Torres VF. Optimization of room-and-pillar dimensions using automated numerical models. Int J Mining Sci Technol 2019;29(5):797–801. http://dx.doi.org/10.1016/j.ijmst.2019.02.003.

[17] Ullah Z, Augarde CE. Finite deformation elasto-plastic modelling using an adaptive meshless method. Comput Struct 2013;118:39–52. http://dx.doi.org/10.1016/j.compstruc.2012.04.001.

[18] Talebi H, Saputra A, Song C. Stress analysis of 3D complex geometry using the scaled boundary polyhedral finite elements. Comput Mech 2016;58:697–715.

[19] Lopes PCF, Pereira AMB, Clua EWG, Leiderman R. A GPU implementaion of the PCG method for large-scale-based finite element analysis in heterogeneous periodic media. Comput Methods Appl Mech Eng 2022;399:115276.

[20] Song C. The scaled boundary finite element method: Introduction to theory and implementation. Wiley; 2018, http://dx.doi.org/10.1002/9781119388487.

[21] Ooi ET, Song C, Natarajan S. A scaled boundary finite element formulation for poroelasticity. Internat J Numer Methods Engrg 2018;114(8):905–29. http://dx.doi.org/10.1002/nme.5770.

[22] Neto EAd, Peric D, Owen DRJ. Computational methods for plasticity: Theory and applications. John Wiley and Sons Ltd; 2008.

[23] Le TMH, Gallipoli D, Sanchez M, Wheeler S. Characteristics of failure mass and safety factor during rainfall of an unsaturated slope. In: E3S web of conferences, vol. 9, 2016, p. 15011.